Manipulating the metal-to-insulator transition and magnetic properties in manganite thin films via epitaxial strain

Dong Li,[1,*] Bonan Zhu,[2,*] Dirk Backes,[3] Larissa S. I. Veiga,[3] Tien-Lin Lee,[3] Hongguang Wang,[4] Qian He,[5] Pinku Roy,[6,7] Jiaye Zhang,[8] Jueli Shi,[8] Aiping Chen,[6] Peter A. van Aken,[4] Quanxi Jia,[7] Sarnjeet S. Dhesi,[3] David O. Scanlon,[2,3] Kelvin H. L. Zhang,[8,†] and Weiwei Li[1,†]

[1]*College of Physics, MIIT Key Laboratory of Aerospace Information Materials and Physics, Nanjing University of Aeronautics and Astronautics, Nanjing 211106, China*

[2]*Department of Chemistry, University College London, London WC1H 0AJ, United Kingdom*

[3]*Diamond Light Source Ltd., Harwell Science and Innovation Campus, Didcot, Oxfordshire OX11 0DE, United Kingdom*

[4]*Max Planck Institute for Solid State Research, Heisenbergstrasse 1, 70569, Stuttgart, Germany*

[5]*Department of Materials Science & Engineering, National University of Singapore, Singapore, 117575, Singapore*

[6]*Center for Integrated Nanotechnologies (CINT), Los Alamos National Laboratory, Los Alamos, New Mexico 87545, USA*

[7]*Department of Materials Design and Innovation, University at Buffalo - The State University of New York, Buffalo, New York 14260, USA*

[8]*State Key Laboratory of Physical Chemistry of Solid Surfaces, Collaborative Innovation Center of Chemistry for Energy Materials, College of Chemistry and Chemical Engineering, Xiamen University, Xiamen 361005, China*

(Received 10 January 2022; revised 6 April 2022; accepted 8 April 2022; published 22 April 2022)

Strain engineering of epitaxial transition metal oxide heterostructures offers an intriguing opportunity to control electronic structures by modifying the interplay between spin, charge, orbital, and lattice degrees of freedom. Here, we demonstrate that the electronic structure, magnetic and transport properties of $La_{0.9}Ba_{0.1}MnO_3$ thin films can be effectively controlled by epitaxial strain. Spectroscopic studies and first-principles calculations reveal that the orbital occupancy in Mn e_g orbitals can be switched from the $d_{3z^2-r^2}$ orbital to the $d_{x^2-y^2}$ orbital by varying the strain from compressive to tensile. The change of orbital occupancy associated with Mn $3d$-O $2p$ hybridization leads to dramatic modulation of the magnetic and electronic properties of strained $La_{0.9}Ba_{0.1}MnO_3$ thin films. Under moderate tensile strain, an emergent ferromagnetic insulating state with an enhanced ferromagnetic Curie temperature of 215 K is achieved. These findings not only deepen our understanding of electronic structures, magnetic and transport properties in the $La_{0.9}Ba_{0.1}MnO_3$ system, but also demonstrate the use of epitaxial strain as an effective knob to tune the electronic structures and related physical properties for potential spintronic device applications.

DOI: 10.1103/PhysRevB.105.165426

Transition metal oxides (TMOs) are an important class of functional materials that exhibit a diverse set of magnetic, electrical, optical and/or catalytic properties and hold great promise for modern technological applications [1]. Among these TMO materials, the mixed-valence manganite, $La_{1-x}A_xMnO_3$ (A = Ca, Sr, and Ba), has stimulated considerable interest as it hosts a rich spectrum of physical properties such as the colossal magnetoresistance, half metallicity, the spontaneous charge-spin-orbital ordering, and ferromagnetic insulator behavior [2,3]. Recently, manganite oxide thin films and heterostructures have attracted intensive interest, since many novel electronic and magnetic ground states can be engineered using interface effects [4–7], defects [1,8], strain engineering [9,10], and different orientations [11].

Particularly, strain engineering has proved to be a powerful way to tailor the functionalities of manganite oxide thin films and heterostructures due to the strong coupling between the structural degrees of freedom and the correlated order parameters [1]. $La_{0.9}Ba_{0.1}MnO_3$ (LBMO) with a pseudocubic lattice constant of 3.89 Å is an example in this context. Bulk LBMO is a ferromagnetic insulator with a Curie temperature (T_C) of ∼185 K and an orthorhombic structure [12,13]. Owing to the combined magnetic and insulating properties, LBMO has strong potential for the application of spintronic devices such as a spin filter in tunnel magnetoresistance devices [14] and a component in a magnetoelectric composite system [15]. However, when LBMO thin films were grown on (001)-oriented $SrTiO_3$ (STO) substrates, it exhibits a ferromagnetic metallic state with T_C varying from 250 to 295 K [13]. The origin of this ferromagnetic metallic state with enhanced T_C is still not fully understood. Possible explanations are suggested for the orbital reconstructions caused by in-plane tensile strain from the STO substrate [16] and epitaxial strain beyond the interfacial region [13]. In fact, apart from the lightly doped $La_{1-x}Ba_xMnO_3$ thin films, the anomalies of enhanced magnetic and transport properties have been also reported in $LaMnO_3$ and $La_{0.9}Sr_{0.1}MnO_3$ thin films with various thicknesses [17,18]. The origin of such an anomaly is still under debate. Furthermore, previous works [13,16] mainly focused

*These authors contributed equally to this work.
†kelvinzhang@xmu.edu.cn, wl337@nuaa.edu.cn

on the growth of LBMO thin films with a relatively narrow strain window (around ∼0.26%), and at a thickness (above 50 nm) which allowed partial strain relaxation in LBMO thin films. To fully reveal the correlation between the electronic structure, magnetic, and transport properties in LBMO thin films, it is necessary to systematically investigate a range of lattice symmetries to gain a fundamental understanding of the strain-property relationship, where relaxation does not complicate the interpretation of the observed physical responses.

In this study, we investigate the electronic structure, magnetic and transport properties of coherently strained epitaxial LBMO thin films using a range of characterization techniques such as scanning transmission electron microscopy (STEM), x-ray photoemission spectroscopy (XPS), and x-ray absorption spectroscopy (XAS). The experimental results are further supplemented with density functional theory (DFT) calculations. By utilizing the suitable substrates, we could vary the epitaxial strain over a wide range from a compressive strain of −2.57% to a tensile strain of +1.8%. We show that the Mn e_g orbital occupancy, Mn 3*d*-O 2*p* hybridization, magnetic and transport properties of LBMO thin films are strongly modulated by the epitaxial strain. Our results clearly illustrate the key role of strain in mediating the competition of spin, orbital, and lattice entanglement in LBMO and other TMOs.

High-quality LBMO thin films were epitaxially grown on a set of single-crystal substrates, including $LaAlO_3$ (LAO), $NdGaO_3$ (NGO), $(LaAlO_3)_{0.3}$-$(SrAl_{0.5}Ta_{0.5}O_3)_{0.7}$ (LSAT), $SrTiO_3$ (STO), $DyScO_3$ (DSO), and $TbScO_3$ (TSO). Figure 1(a) shows the lattice constants of bulk LBMO and different single-crystal substrates. Films were grown at a temperature of 750 °C at an oxygen partial pressure of 100 mTorr, where the pulsed laser deposition was carried out by a KrF excimer laser (248 nm) at a laser fluence of 1.5 J cm^{-2} and 2 Hz. During the growth, *in situ* reflection high-energy electron-diffraction intensity oscillations were monitored to control the thickness of LBMO layer at 26 unit cells (*uc*). After growth, the films were cooled down to room temperature under an oxygen pressure of 300 Torr. The crystal structures and surface morphologies of the films were characterized by high-resolution x-ray diffraction (XRD) with Cu K_α radiation ($\lambda = 1.5405$ Å) (Empyrean, PANalytical) and atomic force microscopy (AFM), respectively. Transmission electron microscopy (TEM) specimens in cross-sectional orientation were prepared by tripod polishing followed by argon ion milling at liquid nitrogen temperature [19]. High-angle annular dark-field (HAADF) STEM images were taken using a JEOL ARM200F and a Nion UltraSTEM operating at 200 kV, equipped with the cold field-emission electron gun and the spherical aberration corrector. Soft XPS was undertaken by a monochromatic Al Kα x-ray source ($h\nu = 1486.6$ eV) using a SPECS PHOIBOS 150 electron energy analyzer with a total energy resolution of 0.5 eV. The Fermi level of the LBMO films was calibrated using a polycrystalline Au foil. Hard x-ray photoelectron spectroscopy (HAXPES) measurements were performed using 5930 keV photon energy at the I09 beamline of the Diamond Light Source. HAXPES spectra were energy-resolved and measured using a VG Scienta EW4000 high-energy analyzer. XAS measurements with polarization dependence were performed at the I06 beamline of the Diamond Light Source. X-ray magnetic circular dichroism

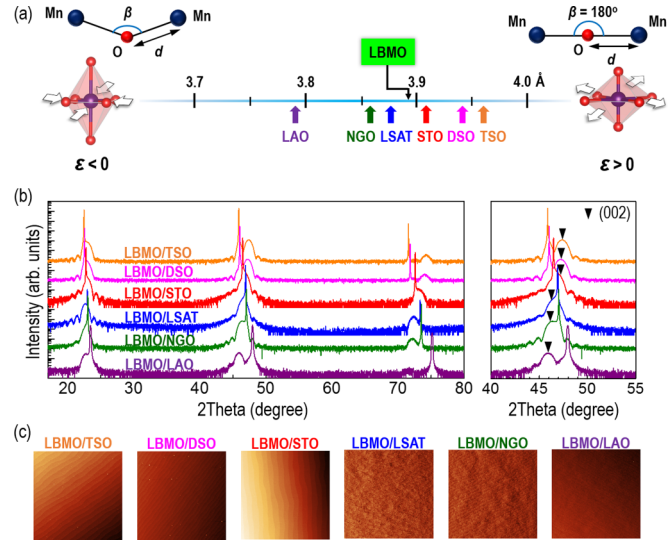

FIG. 1. (a) Top panel: The in-plane bond angle (Mn-O-Mn) β and the bond length (Mn-O) d. Bottom panel: Lattice constants of the LBMO bulk and different single-crystal substrates [LAO: 3.790 Å, NGO: 3.864 Å, LSAT: 3.868 Å, STO: 3.905 Å, DSO: 3.943 Å, and TSO: 3.960 Å]. Pseudocubic lattice constants were used for noncubic single-crystal substrates. (b) Left panel: XRD $\theta-2\theta$ scans of LBMO thin films grown on various substrates. Right panel: XRD $\theta-2\theta$ detailed scans around the (002) reflection. "▼" was used to label the (002) peaks of LBMO thin films. The misfit strain of LBMO thin films gradually changes from a compressive (LAO, NGO, and LSAT) to a tensile strain (STO, DSO, and TSO). (c) Typical 5 × 5-μm AFM height images of LBMO thin films grown on various substrates.

(XMCD) measurements were carried out by probing the total electron yield (TEY) in grazing incidence geometry. XMCD measurements were performed at 2 K under a 6 T magnetic field applied along the *a*-*b* plane of the films, parallel to the beam propagation direction. To ensure that the XMCD signal is of magnetic origin, the magnetic field was also applied in the opposite direction to verify that the sign of the XMCD reversed. X-ray linear dichroism (XLD) measurements were carried out at 300 K without a magnetic field while the TEY was detected in grazing incidence geometry. The XLD spectra were obtained by the intensity difference (I_v-I_h) between the spectra measured with horizontal (E_h) and vertical (E_v) linear polarizations. Macroscopic magnetic measurements were performed with a MPMS3 superconducting quantum interference device-vibrating sample magnetometer (Quantum Design). The magnetic field was applied parallel to the film plane during the measurements. Transport measurements were measured by a Quantum Design Physical Property Measurement System. Plane-wave pseudopotential DFT calculations were carried out using the Vienna *Ab initio* Simulation Package [20,21] (VASP) 5.4.4 with a plane wave cut off energy of 550 eV, γ-centered K-point grids with reciprocal space spacing of 0.314 Å and the Perdew-Burke-Ernzerhof (PBE) exchange-correlation functional [21]. The projector augmented wave [22] method is used with Mn, La, O, Ba potentials from the VASP PBE_54 dataset. The Hubbard U correction [23] is applied to Mn 3*d* electrons with $U_{\text{eff}} = 3.9$ eV [24] to reduce the self-interaction errors

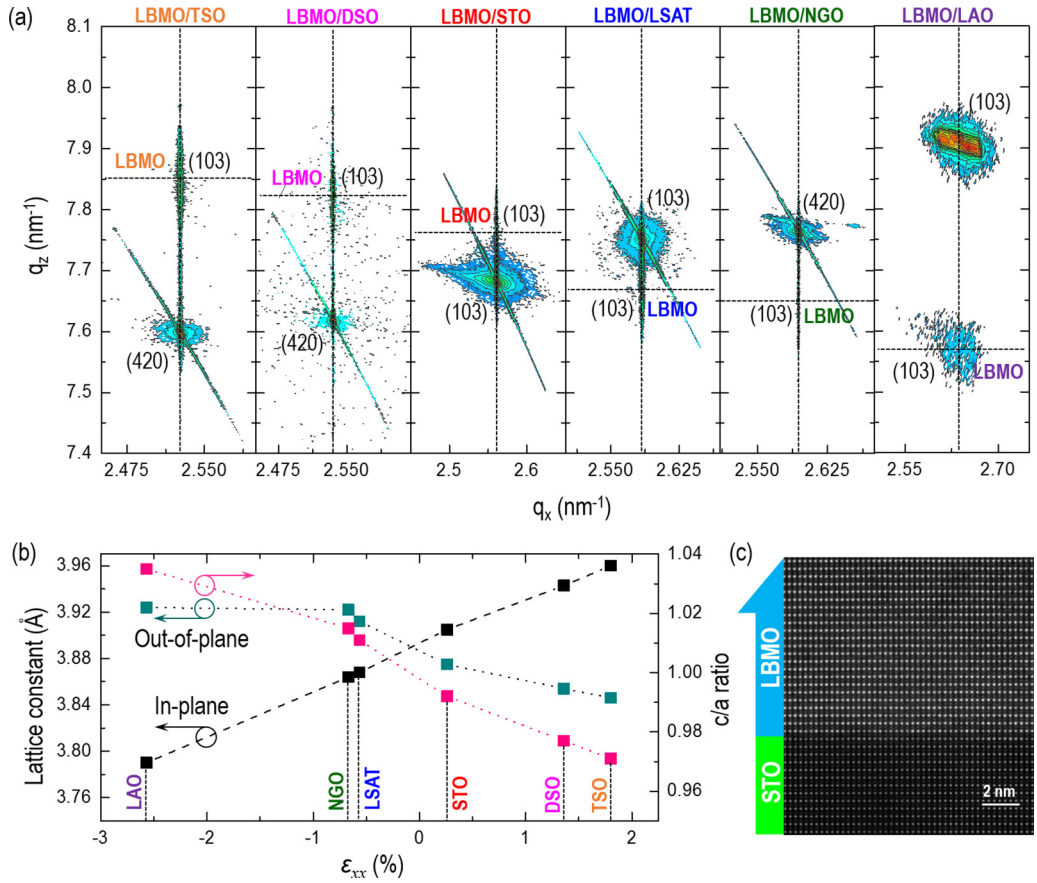

FIG. 2. (a) Reciprocal space maps around the (103) Brag reflection of LBMO thin films grown on various substrates. (b) In-plane and out-of-plane lattice constants and c/a ratio as a function of misfit strains. (c) HAADF STEM image of LBMO thin film grown on STO substrate, viewed from the pseudocubic [110] direction.

known to overly delocalized *d* electrons of transition metals in standard DFT calculations. LBMO structures are constructed from the orthorhombic $LaMnO_3$ unit cells by replacing one in eight La atoms by Ba, giving an effective composition of $La_{0.875}Ba_{0.125}MnO_3$. To simulate epitaxial strain, the *a* and *b* lattice constants are fixed during the relaxation, and only the *c* lattice constant is allowed to change. The AiiDA [25] framework is used to manage the DFT calculations and preserve the provenance. Occupations of the e_g orbitals are computed by summing the projected density of states up to the Fermi level.

Typical out-of-plane XRD θ-2θ scans of the LBMO thin films grown on various substrates show distinct Kiessig fringes around Bragg peaks as presented in Fig. 1(b), indicating a good crystalline quality for all LBMO thin films with long-range periodicity and without any impurity phases. Atomically smooth films' surfaces with a well-defined terrace structure and one-unit-cell steps (∼0.4 nm) were further confirmed by *ex situ* AFM images as shown in Fig. 1(c). To determine the lattice strain of the films, reciprocal space maps (RSMs) were measured and are displayed in Fig. 2(a) and Fig. S1 [35]. The RSMs clearly suggest that all LBMO thin films are coherently strained to the substrates with negligible strain relaxation. The in-plane misfit strain (ε_{xx}) of the LBMO thin films is calculated to be from −2.57% (compressive strain for LBMO on LAO substrate) to +1.8% (tensile strain for LBMO on TSO substrate). Based on the results of XRD θ-2θ and RSMs, strain-dependent in-plane and out-of-plane lattice constants (*a* and *c*), and *c*/*a* ratio are summarized in Fig. 2(b). Figure 2(c) shows the HAADF STEM image of the LBMO thin film grown on STO substrate viewed from s pseudocubic [110] direction, confirming the high-quality of the film with an atomically sharp interface between the film and substrate. In addition, with the increase of compressive or tensile strain as shown in Fig. S2, a small amount of misfit dislocations is formed at the interface between the LBMO thin films and LAO/TSO substrates to relax the strain resulted from the large lattice mismatch.

We first discuss the influence of strain on the oxidation state of Mn in the LBMO thin films using high-resolution XPS and XAS. Figure 3(a) shows the spectra of Mn 2*p* core levels measured with photon energies of 1486.6 eV and 5930 eV. The overall line-shapes of Mn 2*p* core levels agree with the reported spectra of $La_{1-x}Ba_xMnO_3$ [26] and $La_{1-x}Sr_xMnO_3$ [27], displaying the coexistence of Mn^{3+} and Mn^{4+} multiplets. More importantly, it should be noted that there is no visible change in the peak position of the Mn 2*p* core levels, revealing that the oxidation state of Mn is robust against strain. This observation is further validated by soft XAS measured at Mn *L* edges, as presented in Fig. 3(b). It is clearly seen that Mn $L_{3,2}$ edges retain the same peak position when the strain is changed from compressive to tensile. Interestingly, in the Mn 2*p* core-level HAXPES spectra [Fig. 3(a)], an additional

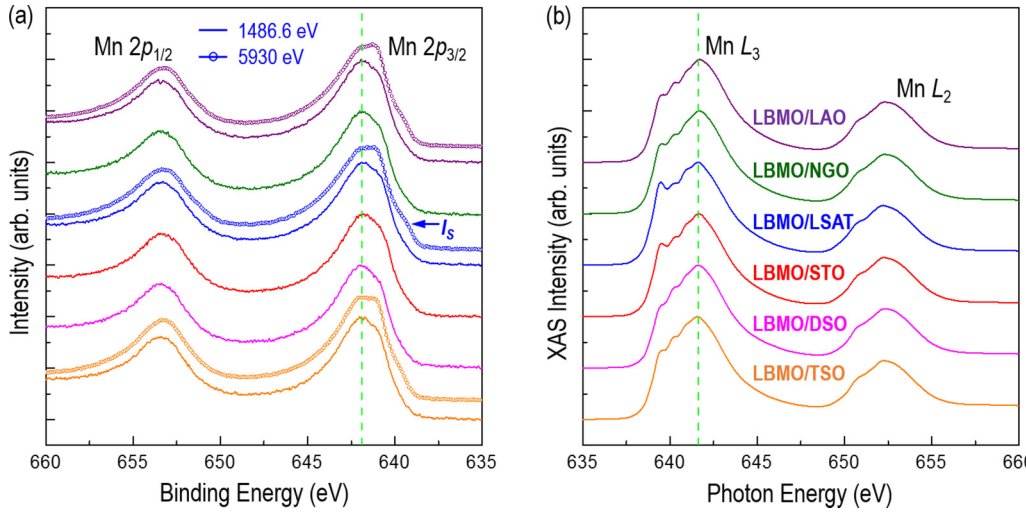

FIG. 3. (a) XPS Mn 2*p* core-level spectra with photon energies of 1486.6 eV (solid lines) and 5930 eV (line and circles), and (b) Mn *L*-edges XAS spectra for LBMO thin films grown on various substrates. The spectra from different samples are shifted for clarification.

shoulder or well-screened structures (I_S) appeared at the low binding energy side (∼639.4 eV) of the Mn $2p_{3/2}$ main peak. According to the previous reports [26,28], the intensity of I_S is strongly related to the strength of ferromagnetic interaction and the magnitude of metallicity in $La_{0.85}Ba_{0.15}MnO_3$ thin films with various thicknesses. Here, we found that the intensity of I_S in LBMO thin films is firstly increased with the decrease of the compressive strain, i.e., from the LBMO thin film grown on the LAO substrate to the LBMO thin film grown on the LSAT substrate. In contrast, I_S disappears under the tensile strain for the LBMO thin film grown on the TSO substrate. This strongly suggests that the magnitude of ferromagnetic magnetization and metallicity in LBMO thin films can be changed by the corresponding epitaxial strain.

To further elucidate the effect of strain on the electronic structures, we carried out the measurements of XPS valence band (VB) and XAS at the O *K* edge to probe the occupied and unoccupied density of states (DOS) near the Fermi level (E_f). As shown in Fig. 4(a), the XPS VB spectra measured with photon energies of 1486.6 eV and 5930 eV mainly consist of four features, as labeled A, B, C, and D. In comparison with resonant photoemission spectra of $La_{0.6}Sr_{0.4}MnO_3$ [27] and $La_{0.7}Sr_{0.3}MnO_3$ [29] films, the intensity of the C and D features originates from the Mn 3*d* states and can be assigned as the t_{2g} and e_g states, respectively. On the other hand, the strongly hybridized states of Mn 3*d* and O 2*p* are responsible for forming the *A* and *B* features. Both soft XPS and HAXPES VB spectra show that a visible DOS is observed across E_f in the energy range of −0.5 to 0.5 eV for the LBMO thin films grown on LAO, NGO, LSAT, and STO substrates, suggestive of a metallic state. On the other hand, for the LBMO thin films grown on DSO and TSO substrates, the VB

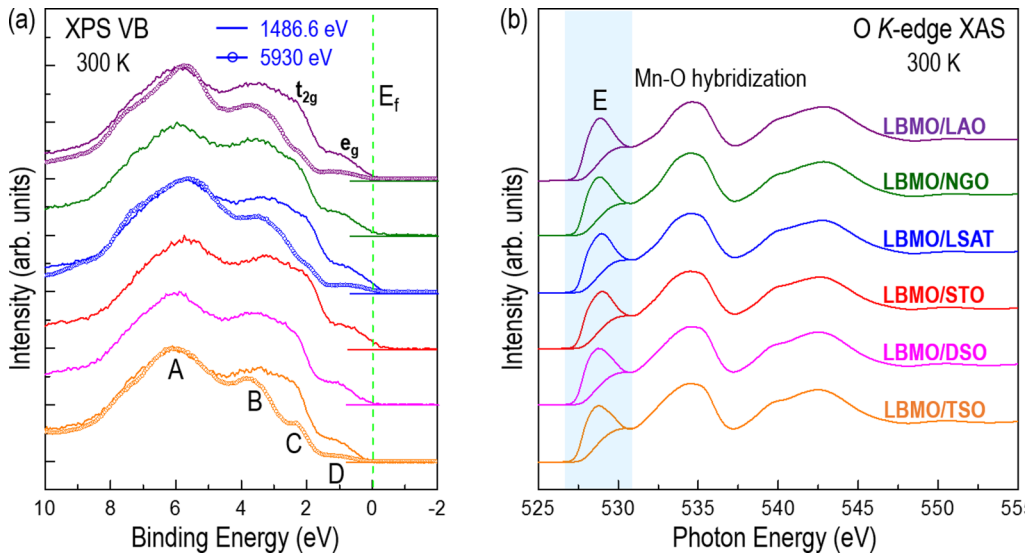

FIG. 4. (a) XPS valence band (VB) spectra excited with photon energies of 1486.6 eV (solid lines) and 5930 eV (line and circles), and (b) O *K*-edge XAS spectra for LBMO thin films grown on various substrates.

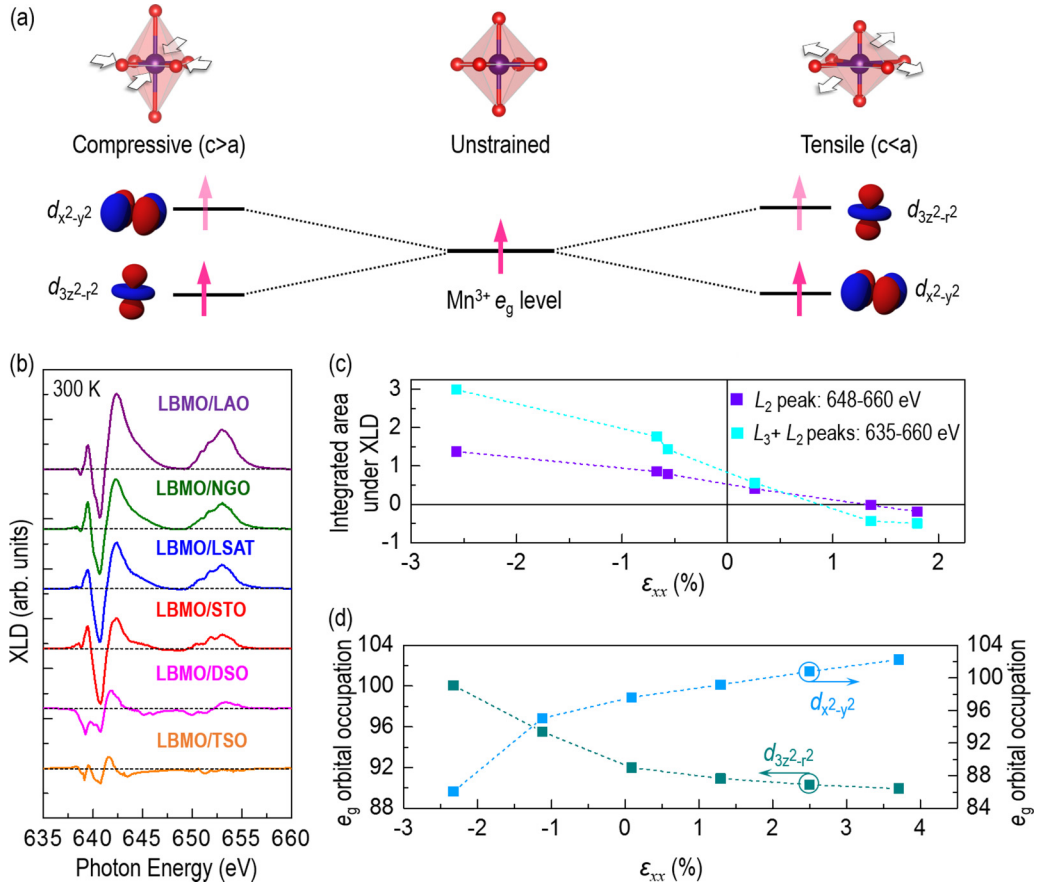

FIG. 5. (a) Top panel: Representation of the MnO_6 octahedral distortions as a function of misfit strain. Bottom panel: Schematic electronic configurations of e_g band in the Mn^{3+} ions. In bulk LBMO (unstrained), the e_g band does not split. When the LBMO thin films are tensile strained, the energy of the $d_{x^2-y^2}$ band is lower, thus holes occupy the $d_{3z^2-r^2}$ band; the opposite trend occurs when the LBMO thin films are under compressive strain. (b) XLD spectra of LBMO thin films grown on various substrates. (c) Integrated area of XLD signal as a function of misfit strain. (d) e_g orbital occupation calculated using DFT as a function of misfit strain.

maximum (VBM) moves away from E_f, and negligible DOS retains at E_f. This, thereby, drives LBMO thin films toward an insulating or semiconducting state. An enlarged view of the VB spectra near E_f is shown in Fig. S3, where the VBM values were determined by linear extrapolation of the leading edge of the VB region to the extended baseline of the VB spectra. The values of VBM are estimated to be −0.06(5) eV for LBMO/LAO, −0.07(5) eV for LBMO/NGO, −0.15(5) eV for LBMO/LSAT, −0.08(5) eV for LBMO/STO, 0.07(5) eV for LBMO/DSO, and 0.11(5) eV for LBMO/TSO. These results further confirm that the LBMO thin films change from a metallic state to an insulating state by varying the strain from compressive to tensile. O K-edge XAS spectra shown in Fig. 4(b) probe the unoccupied states with partial O $2p$ feature hybridized with Mn $3d$ states, La $5d$ states, and Mn $4sp$ states. Hence, O K-edge XAS spectra can be qualitatively related to the unoccupied DOS above E_f [6,7,30,31]. The overall line-shapes of O K-edge XAS spectra of LBMO thin films are consistent with the reported spectra of $La_{1-x}Sr_xMnO_3$ [32–34]. The unoccupied states marked as "E" in the O K-edge XAS spectra are associated with unoccupied Mn $3d$ states hybridized with O $2p$. Using the method developed by Suntivich *et al.* [35], the Mn $3d$-O $2p$ hybridization parameter was quantitatively determined and is presented in Fig. S4. It can be seen that the degree of Mn $3d$-O $2p$ hybridization decreases with the change of strain from compressive to tensile. The occupied DOS measured by XPS VB spectra and unoccupied DOS obtained by O K-edge XAS spectra for LBMO thin films suggest the key electronic modulations induced by strain manipulation.

The orbital occupancy of LBMO thin films was further investigated by XLD using in-plane (I_{ip}) and out-of-plane (I_{oop}) linearly polarized x-ray beams. The absorption of x-ray polarized along E_{ip}//ab (or E_{oop}//c) arises largely from the unoccupied Mn $d_{x^2-y^2}$ (or $d_{3z^2-r^2}$), i.e., the holes [9,36]. As shown in Fig. 5(a), no XLD signal for the unstrained bulk LBMO is expected because of a degenerated orbital occupancy. For LBMO thin films under compressive strain, the electrons preferentially occupy the $d_{3z^2-r^2}$ orbital in e_g orbital. Consequently, the XLD peaks show positive values for the compressive-strained LBMO thin films. In contrast, the e_g orbital of tensile-strained LBMO thin films is occupied by the $d_{x^2-y^2}$ orbital, suggesting negative values for the XLD peaks. Obviously, the line shapes of XLD spectra strongly depend on the strain states of LBMO thin films, as shown in Fig. 5(b). To quantify the orbital occupancy, the integrated areas under the L_2 absorption peak (648–660 eV) and the $L_3 + L_2$ (635–660 eV) in the XLD spectra were evaluated and

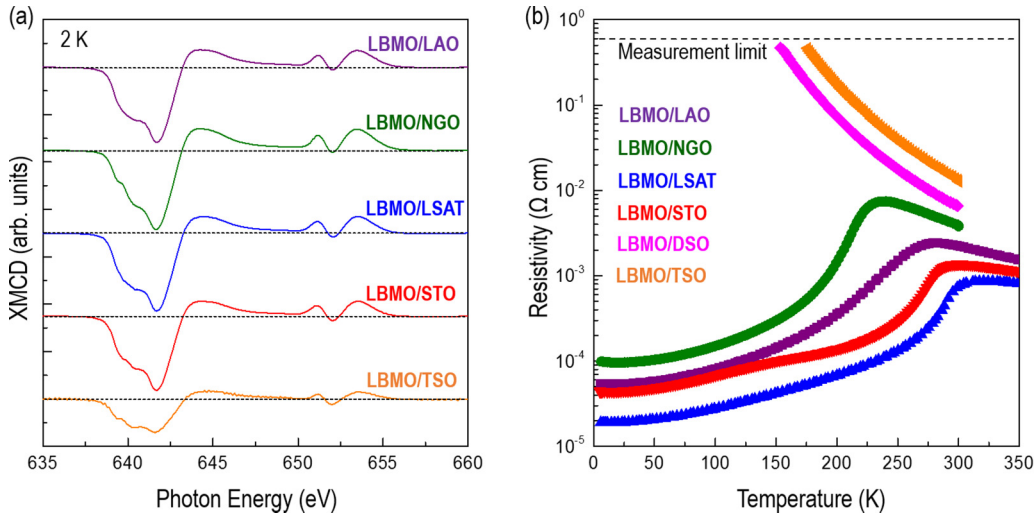

FIG. 6. (a) XMCD spectra and (b) temperature-dependent resistivity of LBMO thin films grown on various substrates.

displayed in Fig. 5(c). The data reveals that the orbital occupancy is switched from the $d_{3z^2-r^2}$ orbital to the $d_{x^2-y^2}$ orbital, when the strain is changed from compressive to tensile. DFT calculations further support the observation of experimental results, as shown in Fig. 5(d). The occupation of the $d_{3z^2-r^2}$ orbital decreases with increasing tensile strain, while that of the $d_{x^2-y^2}$ orbital increases. DFT relaxed structures are known to have systematic errors in the lattice constants, hence the theoretical strain at which the switching happens is not expected to be exactly the same as the experimental one, but the general trend remains consistent.

Owing to the strain-modulated electronic structures and orbital occupancy, we also observed a pronounced modification of magnetic and transport properties. Temperature-dependent magnetization measurements are shown in Fig. S4. With the increase of temperature, the magnetization curves for LBMO thin films show distinct ferromagnetic transition temperatures. Also, we found that the change of strain strongly affects the ferromagnetic T_Cs. To further confirm the observed ferromagnetism, we performed the XMCD at Mn L edges for all LBMO thin films covering the whole range of misfit strain. Previous work has validated that the XMCD can detect the subtle ($\sim 0.005\,\mu_B$/atom) and element-specific magnetic moment [37]. This means that XMCD can exclude the contribution from magnetic impurities. For XMCD measurements, a field of ± 6 T was applied along the in-plane direction at 2 K. XMCD signals were observed for all samples, as presented in Fig. 6(a), except for the LBMO thin film grown on a DSO substrate. This may be caused by the highly resistive nature of the sample at low temperature, prohibiting the detection of a reliable signal in TEY mode. The signals at Mn L_2- and L_3 edges in Fig. 6(a) have opposite signs. We also confirmed that the XMCD signals flip sign with the reversal of the applied magnetic fields (± 6 T). The line shapes of XMCD spectra agree well with the reported data for $La_{0.7}Sr_{0.3}MnO_3$ and $LaMnO_3$ thin films [20,28]. We can see that XMCD spectra clearly show strong dichroism, indicating a net ferromagnetic moment associated with Mn cations in the LBMO thin films grown on various substrates. Temperature-dependent resistivity curves for all samples are displayed in Fig. 6(b). We found that the LBMO thin films grown on LAO, NGO, LAST, and STO substrates exhibit metal-to-insulator transitions (T_{MI}) and their T_{MI}s are consistent with the corresponding T_Cs obtained from temperature-dependent magnetization curves (Fig. S5). Also, note that the LBMO thin films grown on DSO and TSO substrates show an insulating behavior, indicating the films possessing ferromagnetic insulating properties. Furthermore, resulting from the change of compressive strain to tensile strain, the change from a metallic state to an insulating state agrees well with the observation of HAXPES Mn $2p$ core-level spectra [Fig. 3(a)] and VB spectra [Fig. 4(a)].

To gain further insights into the relationship between the strain and its link to the electronic structures, magnetic and transport properties, a phase diagram is constructed and illustrated in Fig. 7. When the applied strain is changed from compressive to tensile, the Mn e_g orbital occupancy

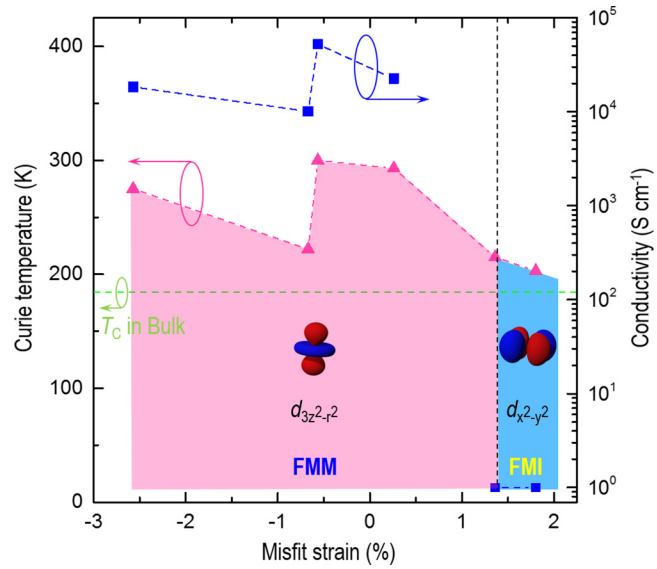

FIG. 7. Misfit strain-dependent ferromagnetic Curie temperature (T_C, left) and the residual conductivity at 5 K (right).

is switched from the $d_{3z^2-r^2}$ orbital to the $d_{x^2-y^2}$ orbital [Figs. 5(c) and 5(d)]. Consequently, ferromagnetic metallic behavior is changed to ferromagnetic insulating (FMI) behavior. We also note that there is a clear change in ferromagnetic T_C for LBMO thin films grown on NGO and LSAT substrates. This could be attributed to the subtle completion between the Mn-O-Mn bond angles and the Mn-O-Mn bond lengths of LBMO thin films with orthorhombic and tetragonal structures (Fig. S1). Additionally, the decrease of ferromagnetic T_C with the further increase of tensile or compressive strain for LBMO thin films grown on TSO and LAO substrates could be caused by the formation of misfit dislocations at the thin film and substrate interface (Fig. S2). More importantly, similar to the bulk LBMO with the FMI behavior, a ferromagnetic insulating state can be achieved in the LBMO thin films under slightly higher tensile strain. Furthermore, the ferromagnetic T_C is enhanced to be a value around 215 K for LBMO thin film grown on DSO substrate, which is higher than that of bulk LBMO (185 K). The underlying physical mechanism of such enhancement in the ferromagnetic T_C could be originated from the increase of the Mn-O-Mn bond angles by applying a moderate tensile strain. Moreover, the ferromagnetic T_C of 215 K is much higher than other widely studied ferromagnetic insulating TMOs such as EuO ($T_C \sim 69.3$ K) [38], $LaCoO_3$ ($T_C \sim 85$ K) [39], and $BiMnO_3$ ($T_C \sim 105$ K) [14]. Therefore, the LBMO thin film with a ferromagnetic insulating state and higher T_C is attractive for the use of designing spintronic devices such as a spin filter in tunnel magnetoresistance devices [14] or a component in a magnetoelectric composite system [15].

In summary, strain effects on the electronic structure, magnetic and transport properties of epitaxial LBMO thin films were systematically investigated using a series of x-ray spectroscopic studies and DFT calculations. Through the manipulation of strain from compressive to tensile, the orbital occupation in Mn e_g can be effectively switched between the $d_{3z^2-r^2}$ orbital and the $d_{x^2-y^2}$ orbital. In addition, the intensity of DOS at E_f gradually disappears and the Mn $3d$-O $2p$ hybridization is reduced. Consequently, under a moderate tensile strain, an emergent ferromagnetic insulating state is realized in the LBMO thin film with an enhanced T_C of 215 K, which is higher than that of bulk LBMO (185 K). Our work suggests a powerful pathway to tailor the physical properties through strain engineering that effectively manipulates the electronic structures and magnetic properties of TMOs for potential spintronic applications.

W.-W.L. acknowledges support from the National Natural Science Foundation of China (Grant No. 52102177), the National Natural Science Foundation of Jiangsu Province (Grant No. BK20210313), Top-notch Academic Programs Project of Jiangsu Higher Education Institutions (TAPP), and the Jiangsu Specially-Appointed Professor Program. K.H.L.Z. is grateful for funding support from the National Natural Science Foundation of China (Grants No. 21872116 and No. 22075232). We thank Diamond Light Source for time on beamline I06 (proposal MM25425, MM26901, and MM29616) and beamline I09 (proposal SI31069). D.O.S. acknowledges support from the European Research Council (Grant 758345). Through our membership of the UK's HEC Materials Chemistry Consortium, which is funded by EPSRC (EP/L000202, EP/R029431, EP/T022213), this work used the ARCHER UK National Supercomputing Service [40], the UK Materials and Molecular Modelling Hub which is partially funded by EPSRC (EP/P020194 and EP/T022213). The authors also acknowledge the use of the UCL Myriad and Kathleen High Performance Computing Facility (Myriad@UCL, Kathleen@UCL), and associated support services, in the completion of this work. The work at Los Alamos National Laboratory was supported by the NNSA's Laboratory Directed Research and Development Program and was performed, in part, at the Center for Integrated Nanotechnologies (CINT), an Office of Science User Facility operated for the U.S. Department of Energy Office of Science. Los Alamos National Laboratory, an affirmative action equal opportunity employer, is managed by Triad National Security, LLC for the U.S. Department of Energy's NNSA, under contract 89233218CNA000001. Q.H. would like to acknowledge the support by National Research Foundation (NRF) Singapore, under its NRF Fellowship (NRF-NRFF11-2019-0002). The work at University at Buffalo was partially supported by the U.S. National Science Foundation under Award No. ECCS-1902623. Q.X.J. also acknowledges the CINT Users Program. We acknowledge U. Salzberger for the TEM sample preparation. This project has received funding from the European Union's Horizon 2020 research and innovation programme under Grant agreement No. 823717-ESTEEM3.

[1] W.-W. Li, J. Shi, K. H. L. Zhang, and J. L. MacManus-Driscoll, Mater. Horiz. **7**, 2832 (2020).

[2] A.-M. Haghiri-Gosent and J.-P. Renard, J. Phys. D **36**, R127 (2003).

[3] H. Yamada, Y. Ogawa, Y. Ishii, H. Sato, M. Kawasaki, H. Akoh, and Y. Tokura, Science **305**, 646 (2004).

[4] A. Tebano, C. Aruta, S. Sanna, P. G. Medaglia, G. Balestrino, A. A. Sidorenko, R. De Renzi, G. Ghiringhelli, L. Braicovich, V. Bisogni, and N. B. Brookes, Phys. Rev. Lett. **100**, 137401 (2008).

[5] P. Yu, J.-S. Lee, S. Okamoto, M. D. Rossell, M. Huijben, C.-H. Yang, Q. He, J. X. Zhang, S. Y. Yang, M. J. Lee, Q. M. Ramasse, R. Erni, Y.-H. Chu, D. A. Arena, C.-C. Kao, L. W. Martin, and R. Ramesh, Phys. Rev. Lett. **105**, 027201 (2010).

[6] W.-W. Li, B. Zhu, Q. He, A. Y. Borisevich, C. Yun, R. Wu, P. Lu, Z. Qi, Q. Wang, A. Chen, H. Wang, S. A. Cavill, K. H. L. Zhang, and J. L. MacManus-Driscoll, Adv. Sci. **7**, 1901606 (2020).

[7] W.-W. Li, B. Zhu, R. Zhu, Q. Wang, P. Lu, Y. Sun, C. Cafolla, Z. Qi, A. Chen, P. Gao, H. Wang, Q. He, K. H. L. Zhang, and J. L. MacManus-Driscoll, Adv. Funct. Mater. **30**, 2001984 (2020).

[8] L. Gao, O. Petracic, P. Zakalek, A. Weber, U. Rücker, J. Schubert, A. Koutsioubas, S. Mattauch, and T. Brückel, Adv. Mater. **31**, 1806183 (2019).

[9] D. Pesquera, G. Herranz, A. Barla, E. Pellegrin, F. Bondino, E. Magnano, F. Sánchez, and J. Fontcuberta, Nat. Commun. **3**, 1189 (2012).

[10] S. K. Giri, J. L. MacManus-Driscoll, W.-W. Li, R. Wu, T. K. Nath, and T. S. Maity, J. Phys. D **52**, 165302 (2019).

[11] L. Ye, D. Zhang, J. Lu, S. Xu, R. Xu, J. Fan, R. Tang, H. Wang, H. Guo, W.-W. Li, and H. Yang, J. Phys. D **55**, 224002 (2022).

[12] B. Dabrowski, K. Rogacki, X. Xiong, P. W. Klamut, R. Dybzinski, J. Shaffer, and J. D. Jorgensen, Phys. Rev. B **58**, 2716 (1998).

[13] J. Zhang, H. Tanaka, T. Kanki, J.-H. Choi, and T. Kawai, Phys. Rev. B **64**, 184404 (2001).

[14] M. Gajek, M. Bibes, A. Bathélémy, K. Bouzehouane, S. Fusil, M. Varela, J. Fontcuberta, and A. Fert, Phys. Rev. B **72**, 020406(R) (2005).

[15] J. Huang, W.-W. Li, H. Yang, and J. L. MacManus-Driscoll, MRS Bull. **46**, 159 (2021).

[16] T. Kanki, H. Tanaka, and T. Kawai, Phys. Rev. B **64**, 224418 (2001).

[17] Z. H. Chen, Z. H. Chen, Z. Q. Liu, M. E. Holtz, C. J. Li, X. Renshaw Wang, W. M. Lü, M. Motapothula, L. S. Fan, J. A. Turcaud, L. R. Dedon, C. Frederick, R. J. Xu, R. Gao, A. T. N'Diaye, E. Arenholz, J. A. Mundy, T. Venkatesan, D. A. Muller, L.-W. Wang, J. Liu, and L. W. Martin, Phys. Rev. Lett. **119**, 156801 (2017).

[18] R. Mbatang, D. Xue, E. Enriquez, R. Yuan, H. Han, P. Dowden, Q. Wang, E. Fohtung, D. Xue, T. Lookman, S. J. Pennycook, and A. Chen, Nanoscale **11**, 7364 (2019).

[19] H. Wang, V. Sort, B. Frenk, G. Laskin, J. Mannhart, and P. A. v. Aken, Micron **140**, 102979 (2021).

[20] G. Kresse and J. Furthmüller, Comput. Mater. Sci. **6**, 15 (1996).

[21] G. Kresse and J. Furthmüller, Phys. Rev. B **54**, 11169 (1996).

[22] P. E. Blöchl, Phys. Rev. B **50**, 17953 (1994).

[23] S. L. Dudarev, G. A. Botton, S. Y. Savrasov, C. J. Humphreys, and A. P. Sutton, Phys. Rev. B **57**, 1505 (1998).

[24] L. Wang, T. Maxisch, and G. Ceder, Phys. Rev. B **73**, 195107 (2006).

[25] S. P. Huber, S. Zoupanos, M. Uhrin, L. Talirz, L. Kahle, R. Häuselmann, D. Gresch, T. Müller, A. V. Yakutovich, C. W. Andersen, F. F. Ramirez, C. S. Adorf, F. Gargiulo, S. Kumbhar, E. Passaro, C. Johnston, A. Merkys, A. Cepellotti, N. Mounet, N. Marzari, B. Kozinsky, and G. Pizzi, Sci. Data **7**, 300 (2020).

[26] S. Ueda, H. Tanaka, E. Ikenaga, J. J. Kim, T. Ishikawa, T. Kawai, and K. Kobayashi, Phys. Rev. B **80**, 092402 (2009).

[27] K. Horiba, A. Chijamatsu, H. Kumigashira, M. Oshima, N. Nakagawa, M. Lippmaa, K. Ono, M. Kawasaki, and H. Koinuma, Phys. Rev. B **71**, 155420 (2005).

[28] H. Tanaka, Y. Takata, K. Horiba, M. Taguchi, A. Chainani, S. Shin, D. Miwa, K. Tamasaku, Y. Nishino, T. Ishikawa, E. Ikenaga, M. Awaji, A. Takeuchi, T. Kawai, and K. Kobayashi, Phys. Rev. B **73**, 094403 (2006).

[29] J.-H. Park, E. Vescovo, H.-J. Kim, C. Kwon, R. Ramesh, and T. Venkatesan, Phys. Rev. Lett. **81**, 1953 (1998).

[30] W.-W. Li, K. Jiang, Z. Li, S. Gong, R. L. Z. Hoye, Z. Hu, Y. Song, C. Tian, J. Kim, K. L. Z. Zhang, S. Cho, and J. L. MacManus-Driscoll, Adv. Energy Mater. **8**, 1801972 (2018).

[31] G. Fu, W.-W. Li, J.-Y. Zhang, M. Li, C. Li, N. Li, Q. He, S. Xi, D. Qi, J. L. MacManus-Driscoll, and K. L. Z. Zhang, Small **17**, 2006930 (2021).

[32] M. Abbate, F. M. F. de Groot, J. C. Fuggle, A. Fujimori, O. Strebel, F. Lopez, M. Domke, G. Kaindl, G. A. Sawatzky, M. Takano, Y. Takeda, H. Eisaki, and S. Uchida, Phys. Rev. B **46**, 4511 (1992).

[33] T. Saitoh, A. E. Bocquet, T. Mizokawa, H. Namatame, A. Fujimori, M. Abbate, Y. Takeda, and M. Takano, Phys. Rev. B **51**, 13942 (1995).

[34] A. Galdi, C. Aruta, P. Orgiani, C. Adamo, V. Bisogni, N. B. Brookes, G. Ghiringhelli, D. G. Schlom, P. Thakur, and L. Maritato, Phys. Rev. B **85**, 125129 (2012).

[35] See Supplemental Material at http://link.aps.org/supplemental/10.1103/PhysRevB.105.165426 for determining the Mn 3d-O 2p hybridization parameters for the LBMO thin films as a function of epitaxial strain.

[36] A. Tebano, C. Aruta, S. Sanna, P. G. Medaglia, G. Balestrino, A. A. Sidorenko, R. De Renzi, G. Ghiringhelli, L. Braicovich, V. Bisogni, and N. B. Brookes, Phys. Rev. Lett. **103**, 079902(E) (2009).

[37] C. T. Chen, Y. U. Idzerda, H.-J. Lin, N. V. Smith, G. Meigs, E. Chaban, G. H. Ho, E. Pellegrin, and F. Sette, Phys. Rev. Lett. **75**, 152 (1995).

[38] A. Mauger and C. Godart, Phys. Rep. **141**, 51 (1986).

[39] D. C. Meng, H. L. Guo, Z. Z. Cui, C. Ma, J. Zhao, J. B. Lu, H. Xu, Z. C. Wang, X. Hu, Z. P. Fu, R. R. Peng, J. H. Guo, X. F. Zhao, G. J. Brown, R. Knize, and Y. L. Lu, Proc. Natl. Acad. Sci. USA **115**, 2873 (2018).

[40] http://www.archer.ac.uk